Smart Materials and Structures

PAPER

Effects of superelasticity and plasticity on the spherical indentation response of shape memory alloys: a finite element analysis

To cite this article: J Anuja *et al* 2019 *Smart Mater. Struct.* **28** 035028

View the article online for updates and enhancements.

This content was downloaded from IP address 14.139.128.34 on 04/04/2019 at 06:32

IOP Publishing Smart Materials and Structures
Smart Mater. Struct. **28** (2019) 035028 (18pp) https://doi.org/10.1088/1361-665X/aaff88

Effects of superelasticity and plasticity on the spherical indentation response of shape memory alloys: a finite element analysis

J Anuja[1], R Narasimhan[2] and U Ramamurty[3]

[1] Department of Materials Engineering, Indian Institute of Science, Bangalore, 560012, India
[2] Department of Mechanical Engineering, Indian Institute of Science, Bangalore, 560012, India
[3] School of Mechanical and Aerospace Engineering, 50 Nanyang Avenue, Nanyang Technological University, 639798, Singapore

E-mail: anujaj3891@gmail.com, narasi@iisc.ac.in and satwiku@gmail.com

Received 11 September 2018, revised 25 December 2018
Accepted for publication 17 January 2019
Published 14 February 2019

Abstract

Instrumented indentation is particularly useful for characterizing the mechanical behavior of shape memory alloys (SMAs), which are often used as 'small volume' elements such as thin films or wires. Deciphering the measured indentation response, which is as such difficult for elastic-plastic materials due to the inhomogeneous state of stress underneath the indenter, becomes more complex for SMAs owing to the simultaneous occurrence of stress induced martensite transformation (SIMT) in conjunction with plastic deformation. In this work, a constitutive model that is able to capture the coupled nature of phase transformation and plastic deformation is employed to study, through finite element analyses, the spherical indentation behavior of SMAs at a temperature above the austenite finish temperature, A_f. It is found that the concurrent development of plastic yielding and SIMT leads to slower evolution of martensite volume and a smaller transformed zone size. Also, in the absence of plastic yielding, the proportion of depth recovered by superelasticity is fairly constant. It is also observed, from a systematic comparison with a conventional elastic-plastic material, that the presence of the transformed zone significantly alters the stress distribution beneath the indenter.

Keywords: spherical indentation, shape memory alloys, superelasticity, martensite phase transformation, finite element analysis

(Some figures may appear in colour only in the online journal)

1. Introduction

Shape memory alloys (SMAs) possess the unique ability to recover large values of imposed strain (7%–10%) under suitable thermomechanical loading conditions [1]. Such large strain recovery is intimately linked to the reversible austenite to martensite phase transformation that can be triggered via either a temperature change (referred to as shape memory effect) or by mechanical means (superelasticity, SE), or a combination of both. SE typically occurs when the SMA is strained at temperatures greater than A_f, wherein SIMT occurs upon loading. However, upon unloading, the transformed martensite reverts back to the austenite phase, leading to full recovery of the transformation strain in the absence of plastic yielding. A number of applications of SMAs are designed to exploit these features [2–7].

In a majority of the above mentioned applications, the SMA components used are small in size (for example, in thin films and micro-electro-mechanical systems), and therefore it is difficult to probe and characterize their mechanical and functional responses. Instrumented indentation, because of its ability to quantitatively characterize the small volume mechanical behavior of materials [8], has been extensively used for this purpose [9–21]. Ni *et al* [11] showed that depth recovery upon unloading and recoverable energy ratio measured from indentation load-depth (P–h) responses can be

 © 2019 IOP Publishing Ltd Printed in the UK

used to quantify the magnitude of shape memory and superelastic recovery. An important observation reported by them is that the depth recovery ratio is much higher for spherical indentation than for Berkovich indentation for the same representative strain of 0.08. This difference was attributed to the fact that the maximum equivalent plastic strain is larger underneath sharp as compared to spherical indenters, which impedes the reverse transformation. Similar observations were made by Wood and Clyne [14] from nano-indentation measurements and simulations. Shastry and Ramamurty [20] showed that the depth and work recovery ratios are complementary measures that can be used to gauge the recovery characteristics of SMAs.

A combination of dimensional analysis and finite element (FE) modeling has been used in many studies [15, 16, 18, 19, 21] to develop important relationships between indentation response and material properties. In particular, Kan *et al* [21] developed a numerical method, based on FE studies and dimensional analysis, to determine the elastic modulus of the austenite and martensite phases from spherical indentation tests using the Oliver–Pharr method. They also established that the measured indentation modulus varied with the elastic moduli of the two phases, the indentation depth, the forward transformation stress, the transformation hardening coefficient and the maximum transformation strain.

Despite the widespread use of instrumented indentation to characterize the mechanical response of SMAs, the interpretation of the results obtained still poses a challenge owing to several factors such as an inhomogeneous stress state, concurrent occurrence of SIMT and plastic deformation, etc. It is imperative, therefore, that a thorough understanding of these deformation mechanisms and their influence on various mechanical parameters is obtained through the use of advanced constitutive equations and numerical simulation techniques. In particular, the following key issues need to be addressed.

- Most of the existing simulations on the indentation response of SMAs have employed constitutive models that do not take into account the coupling between SIMT and plastic responses. For example, Zhang *et al* [19] used a constitutive model which stipulated that plastic strain will be generated only if the martensite volume fraction exceeds 95% beyond which the volume fraction itself will not evolve. Experimental evidence, however, points out that these processes occur concurrently and, thus, it is essential to understand its implications with respect to the spherical indentation response [22, 23].
- The contributions of conventional elastic and SE effects on depth recovered during unloading in the absence and presence of plastic deformation has not been ascertained. A fundamental issue here is to clearly identify the stage at which reverse transformation, during unloading begins and ceases (if plastic deformation is taken into account).
- As a first step towards using indentation *P–h* records to deduce the superelastic and plastic properties of SMAs, the mechanics of indentation, for example, the stress distribution underneath the indenter and how it is different as compared to an elastic-plastic material, needs to be examined.

Keeping the above issues in view, FE simulations of spherical indentation of SMAs are carried out in the present study by using a constitutive model that accounts for SE and shape memory effects as well as the concurrent occurrence of plastic deformation. However, attention is restricted to just SE combined with plastic deformation by carrying out the simulations at a fixed temperature above A_f. The material properties pertaining to two Ni–Ti alloys with $A_f = 380$ and 282 K are used in the simulations. The individual effects of plastic deformation and SE as well as their interplay are studied by conducting analyses suppressing either of these deformation modes as well as allowing them to act in unison. It is observed that the size of the fully transformed martensite region is smaller when both these modes operate as compared to when there is no plastic yielding. Also, in the absence of plastic yielding the superelastic depth recovered is constant and independent of the indentation depth. It must be noted that spherical indenter is chosen in this work instead of sharp indenters like Berkovich since it allows for a systematic study of transition from elastic to elastic-plastic deformation. Further, as will be seen from the results of the present simulations, it gives an additional flexibility of investigating the strain associated with SIMT in the case of SMAs. This is because one can vary the net indentation strain in a systematic manner. By contrast, a sharp indenter will induce a fixed and large strain, which is independent of the depth of penetration. This would make inferences from the *P–h* curve difficult.

2. Constitutive model for SMAs

The constitutive model used here was originally proposed by Hartl and Lagoudas [23] within a rate independent, small strain framework. It has been chosen in this work because it is capable of capturing the coupled nature of SIMT and plastic yielding. It has been observed that finite deformation analysis is required to accurately describe the stress fields near the contact area [24, 25]. In order to facilitate easy implementation of the Hartl and Lagoudas model [23] in a finite deformation, **FE** formulation, a rate dependent version is employed using a corotational frame generated by a rotation tensor **R** defined as:

$$\dot{\boldsymbol{R}} = \boldsymbol{w}\boldsymbol{R},\ \boldsymbol{R}(t=0) = \boldsymbol{1}. \tag{1}$$

Here, $\boldsymbol{w} = \mathrm{skew}(\boldsymbol{l})$ is the spin tensor and $\boldsymbol{l} = \boldsymbol{\nabla}_x \boldsymbol{v}$ is the spatial velocity gradient. On defining the Kirchhoff stress with respect to the corotational frame as:

$$\boldsymbol{\tau}^{\boldsymbol{R}} = \boldsymbol{R}^{\boldsymbol{T}}\boldsymbol{\tau}\boldsymbol{R}, \tag{2}$$

it can be shown that the objective Jaumann rate of Kirchhoff stress $\overset{\nabla}{\boldsymbol{\tau}}$ is related to the material time derivative $\dot{\boldsymbol{\tau}}^{\mathbf{R}}$ as:

$$\dot{\boldsymbol{\tau}}^{\boldsymbol{R}} = \boldsymbol{R}^{\boldsymbol{T}}\overset{\nabla}{\boldsymbol{\tau}}\boldsymbol{R}. \tag{3}$$

Hence, as noted by Simo and Hughes [26], the finite

deformation version of the inelastic constitutive model employing $\overset{\nabla}{\boldsymbol{\tau}}$ and elastic rate of deformation $\boldsymbol{d^e}$ is canonically same as the small strain theory if the equations are written in the corotational frame. Hence, all the constitutive equations are presented below in this frame.

The two key state variables in the model are the martensite volume fraction, ξ, and the equivalent plastic strain $\bar{\epsilon}_p$. The material properties like elasticity tensor, the yield stress etc, are defined by rule of mixture using ξ. In the following, a material property represented along with $\sim$ sign over it denotes the difference between the values pertaining to martensite and austenite phases.

An additive decomposition of deformation rate in $\boldsymbol{R}$ frame is assumed as:

$$\boldsymbol{d^R} = \boldsymbol{d^{Re}} + \boldsymbol{d^{Ri}}, \tag{4}$$

where $\boldsymbol{d^{Re}}$ and $\boldsymbol{d^{Ri}}$ are the elastic and inelastic components of the rate of deformation tensor. The latter embodies contribution from both plastic and phase transformation processes so that:

$$\boldsymbol{d^{Ri}} = \boldsymbol{d^{Rp}} + \boldsymbol{d^{Rt}}. \tag{5}$$

As mentioned earlier, a hypoelastic equation which relates $\overset{\nabla}{\boldsymbol{\tau}}^{\boldsymbol{R}}$ and $\boldsymbol{d^{Re}}$ is assumed as:

$$\overset{\nabla}{\boldsymbol{\tau}}^{\boldsymbol{R}} = \boldsymbol{C}(\boldsymbol{\xi})\colon (\boldsymbol{d^{Re}} - \dot{\theta}\alpha \underset{\sim}{1}). \tag{6}$$

Here, θ is the absolute temperature, $\boldsymbol{C}(\boldsymbol{\xi})$ is the effective (isotropic) elasticity tensor and α is the effective thermal conductivity defined as:

$$\boldsymbol{C}(\boldsymbol{\xi}) = \boldsymbol{C^A} + \xi\tilde{\boldsymbol{C}} \text{ and } \alpha = \alpha^A + \xi\tilde{\alpha}. \tag{7}$$

The flow rules for plastic and transformation deformation rates in $\boldsymbol{R}$ frame is given by:

$$\boldsymbol{d^{Rp}} = \dot{\bar{\epsilon}}_p\, \boldsymbol{m_p}(\boldsymbol{\tau^R}), \text{ and,} \tag{8}$$

$$\boldsymbol{d^{Rt}} = \dot{\xi}\, \boldsymbol{m_t}(\boldsymbol{\tau^R}). \tag{9}$$

Here, the plastic flow and transformation tensors are defined in terms of the deviatoric stress as:

$$\begin{aligned} \boldsymbol{m_p} &= 3\boldsymbol{\tau}^{\boldsymbol{R}'}/2\bar{\tau} \text{ and } \boldsymbol{\tau}^{\boldsymbol{R}'} = dev(\tau^{\boldsymbol{R}}), \\ \bar{\tau} &= \sqrt{3/2\boldsymbol{\tau}^{\boldsymbol{R}'}\colon \boldsymbol{\tau}^{\boldsymbol{R}'}}, \text{ and,} \\ \boldsymbol{m_t} &= \begin{Bmatrix} 3/2H_c\boldsymbol{\tau}^{\boldsymbol{R}'}/\bar{\tau}, & \text{for } \dot{\xi} > 0 \\ \boldsymbol{\epsilon_{t-r}}/\xi_{t-r}, & \text{for } \dot{\xi} < 0 \end{Bmatrix}. \end{aligned} \tag{10}$$

In the above equation, the transformation flow tensor during reverse transformation is defined in terms of transformation strain $\boldsymbol{\epsilon_{t-r}}$ and martensite volume fraction ξ_{t-r} at the end of forward transformation [23]. A power law viscous evolution equation for equivalent plastic strain rate $\dot{\bar{\epsilon}}_p$ is assumed as:

$$\dot{\bar{\epsilon}_p} = \dot{\bar{\epsilon}}_0(\bar{\tau}/(Y_p + f_p))^{1/m}. \tag{11}$$

Here, Y_p is the initial yield strength of the material and f_p is the plastic hardening function. The former is written as:

$$Y_p = Y_0^A + \xi\widetilde{Y_0}, \tag{12}$$

where, Y_0^A and Y_0^M are the initial yield strengths of the austenite and martensite phases, respectively. The hardening function is assumed to have a saturation form as:

$$f_p(\xi, \bar{\epsilon}_p) = f_p^A + \xi\widetilde{f_p}, \tag{13}$$

where

$$\begin{aligned} f_p^A &= (Y_m^A - Y_0^A)(1 - e^{-C_H\bar{\epsilon}_p}), \\ f_p^M &= (Y_m^M - Y_0^M)(1 - e^{-C_H\bar{\epsilon}_p}), \text{ and,} \\ \widetilde{f_p} &= f_p^M - f_p^A. \end{aligned} \tag{14}$$

In the above equations, Y_m^A and Y_m^M are the saturation yield strengths of the austenite and martensite phases, respectively, and C_H is a hardening constant. A power law, viscous evolution equation is also assumed for martensite volume fraction, $\dot{\xi}$ as:

$$\dot{\xi} = \dot{\xi}_0(|\pi_t|/Y_t)^{1/m} \tag{15}$$

where π_t is the thermodynamic driving force for phase transformation and is given by:

$$\begin{aligned} &\pi_t = \boldsymbol{\tau^R}\colon \boldsymbol{m_t} + p, \text{ and,} \\ &p = \frac{1}{2}\boldsymbol{\tau^R}\colon \tilde{\boldsymbol{S}}\colon \boldsymbol{\tau^R} - (\tilde{Y}_m - \tilde{Y}_0)(\bar{\epsilon}_p + e^{-C_H\bar{\epsilon}_p}/C_H) \\ &\quad + \rho\tilde{\eta}_0\theta - \rho\tilde{u}_0 - f_t(\xi) - \rho\tilde{c}((\theta - \theta_0) - \theta\ln(\theta/\theta_0)). \end{aligned} \tag{16}$$

In the above equation, η_0 and u_0 represent the entropy and internal energy per unit mass in the reference configuration, c, the specific heat and ρ_0, the reference mass density. Also, $\boldsymbol{S}$ is the compliance tensor and is defined as: $\boldsymbol{S} = \boldsymbol{C}^{-1}(\xi)$. Further, $f_t(\xi)$ is the transformation hardening function and is given by:

$$f_t(\xi) = \begin{Bmatrix} \frac{1}{2}a_1(1 + \xi^{n_1} - (1 - \xi^{n_2})) + a_3, & \dot{\xi} > 0 \\ \frac{1}{2}a_2(1 + \xi^{n_3} - (1 - \xi^{n_4})) - a_3, & \dot{\xi} < 0 \end{Bmatrix}. \tag{17}$$

The form of the above function ensures smooth stress–strain and strain-temperature responses during phase transformation [27]. The degree of the smoothness is decided by the set of parameters, n_i [23]. A lower bound, ξ_{lc}, to which the martensite volume fraction can decrease during unloading, is introduced when plastic yielding and phase transformation have occurred simultaneously during the loading part of the cycle. Thus, upon unloading, reverse transformation will occur as long as $\xi \geqslant \xi_{lc}$. This parameter is defined as:

$$\xi_{lc} = \begin{Bmatrix} \bar{\epsilon}_p/\bar{\epsilon}_{crit}, & \bar{\epsilon}_p < \bar{\epsilon}_{crit} \\ 1, & \bar{\epsilon}_p > \bar{\epsilon}_{crit} \end{Bmatrix}. \tag{18}$$

Here, $\bar{\epsilon}_{crit}$ is a critical plastic strain level such that if $\bar{\epsilon}_p$ exceeds this value, no martensite volume fraction will be recovered.

In the above constitutive model, the primary constants are the Young's Modulus and Poisson's ratio of the austenite and martensite phases: E_A, ν_A, E_M, ν_M, as well as the initial and saturation yield strengths Y_0^A, Y_0^M, Y_m^A, Y_m^M, transformation hardening exponents n_1, n_2, n_3, n_4, reference plastic and

Table 1. Primary constants used in the constitutive model for the two alloys used in the simulations.

Parameter	Alloy 1	Alloy 2
E_A (GPa)	69	72
E_M (GPa)	38	30
$\nu_A = \nu_M$	0.33	0.42
$\alpha_A = \alpha_M$ (K^{-1})	10^{-5}	10^{-5}
M_s (K)	321	254.9
M_f (K)	319	238.8
A_s (K)	373	272.7
A_f (K)	380	281.6
Y_0^A (MPa)	420	400
Y_0^M (MPa)	500	800
Y_M^A (MPa)	1000	900
Y_M^M (MPa)	1050	1000
C_H	80	80
$\bar{\varepsilon}^p_{crit}$	0.022	0.022
H^c	0.06	0.05
m	0.02	0.02
$\dot{\xi}_0 = \dot{\bar{\varepsilon}}_0$ (s^{-1})	0.01	0.01
$\rho\tilde{c}$ (J m^{-3} K^{-1})	0.0	0.0
$n_1 = n_2$	1.0	1.0
$n_3 = n_4$	0.2	0.2

martensite volume fraction rates $\dot{\bar{\varepsilon}}_0$, $\dot{\xi}_0$, rate exponent m, thermal conductivities α_A, α_M, critical plastic strain level $\bar{\varepsilon}_{crit}$ and transformation resistance, Y_t. All these constants along with the austenite and martensite start and finish temperatures A_s, A_f, M_s, M_f and transformation strain pertaining to two Ni–Ti alloys chosen in this study are listed in table 1 [23]. The remaining constants that occur in the above constitutive model are derived following the approach outlined in [23, 28]. It can be noted from table 1 that Alloy 1 has $A_f = 380$K, while Alloy 2 has A_f closer to room temperature ($A_f = 282$ K). Although, the constitutive model has been implemented within a rate-dependent framework here because experimental studies show that Ni–Ti SMAs display strain-rate dependent mechanical behavior [29, 30], a small value of m is assumed in the computations (see table 1) so that the transformation equations are effectively rate independent.

The rate tangent modulus (forward gradient) method, proposed by Peirce *et al* [31] along with the Hughes-Winget algorithm [32], is employed to implement the above model in the general purpose FE code FEAP [33]. The implementation details are given in [34]. It must be noted that the Hughes–Winget algorithm [32] ensures that incremental objectivity is maintained during constitutive update and no spurious stresses arise due to rigid rotations. Several benchmark examples have been analyzed to validate the numerical implementation [34]. The stress–strain responses obtained from numerical simulations of uniaxial loading and unloading tests conducted at reference temperatures, $\theta_0 = 353$ and 418 K, for Alloy 1 are presented in figures 1(a) and (b) along with experimental data given in [23]. In figures 1(c) and (d) evolution histories of martensite volume fraction and equivalent plastic strain obtained from the loading/unloading simulation at $T = 418$ K are shown. The tensile stress–strain response for Alloy 2 obtained from numerical simulations corresponding to $T = 310$ K is presented in figure 1(e) along with the experimental data given in [35]. It may seen from figures 1(a), (b) and (e) that the stress–strain responses predicted by the numerical simulations match reasonably well with the experimental variations. Further, the numerical results shown in figures 1(a)–(d) agree well with those given in [23] where a different constitutive update algorithm was employed within a rate independent framework. However, it can be observed from figure 1(b) that there is some discrepancy in the unloading behavior at $T = 418$ K between the numerically predicted and experimental variations. The stress at which reverse transformation commences during unloading and the extent to which it progresses are the two areas of this discrepancy. It arises because the transformation temperatures show a hysteresis, which is not embodied within the modeling framework. These simulation results along with others such as that pertaining to beam bending (which was compared with [36]) lend confidence to the constitutive update procedure employed in this work. It must be noted that although the plots shown in figure 1 to validate the numerical implementation pertain to uniaxial tension, the constitutive model described above can be used for describing multi-axial stress and strain states such as those occurring underneath an indenter. Also, while a few parameters such as yield strengths and transformation strain are extracted from the unaxial tension experimental data, the rest of the parameters are determined from phase transfromation temperatures and properties [23, 28].

3. Modeling aspects

In this work, finite deformation, FE analyses of spherical indentation are performed at fixed temperatures of $\theta = 418$ K and $\theta = 330$ K for Alloys 1 and 2 respectively (which are greater than A_f), by considering three material models. These pertain to (a) an elastic-plastic material obeying J_2 flow theory of plasticity with properties of austenite phase (see table 1) referred to as EPA, (b) superelastic material suppressing plastic deformation which is denoted as SE and (c) superelastic material including plastic deformation behavior referred to as SEP. These choices enable assessing the individual effects of plastic deformation and phase transformation on the indentation response. It must be noted that the spherical indentation problem can be idealized as axisymmetric due to the isotropic, homogeneous nature of the specimen and the indenter geometry. Thus, a 2D axisymmetric analysis will yield complete information about the 3D character of the stress and strain distributions (involving σ_{rr}, σ_{zz}, τ_{rz} and $\sigma_{\theta\theta}$). In particular, the complex triaxial stress state underneath the indenter can be captured by axisymmetric modeling for the problem studied (see, for example [14, 15, 19, 37] where numerical/analytical solutions for spherical indentation

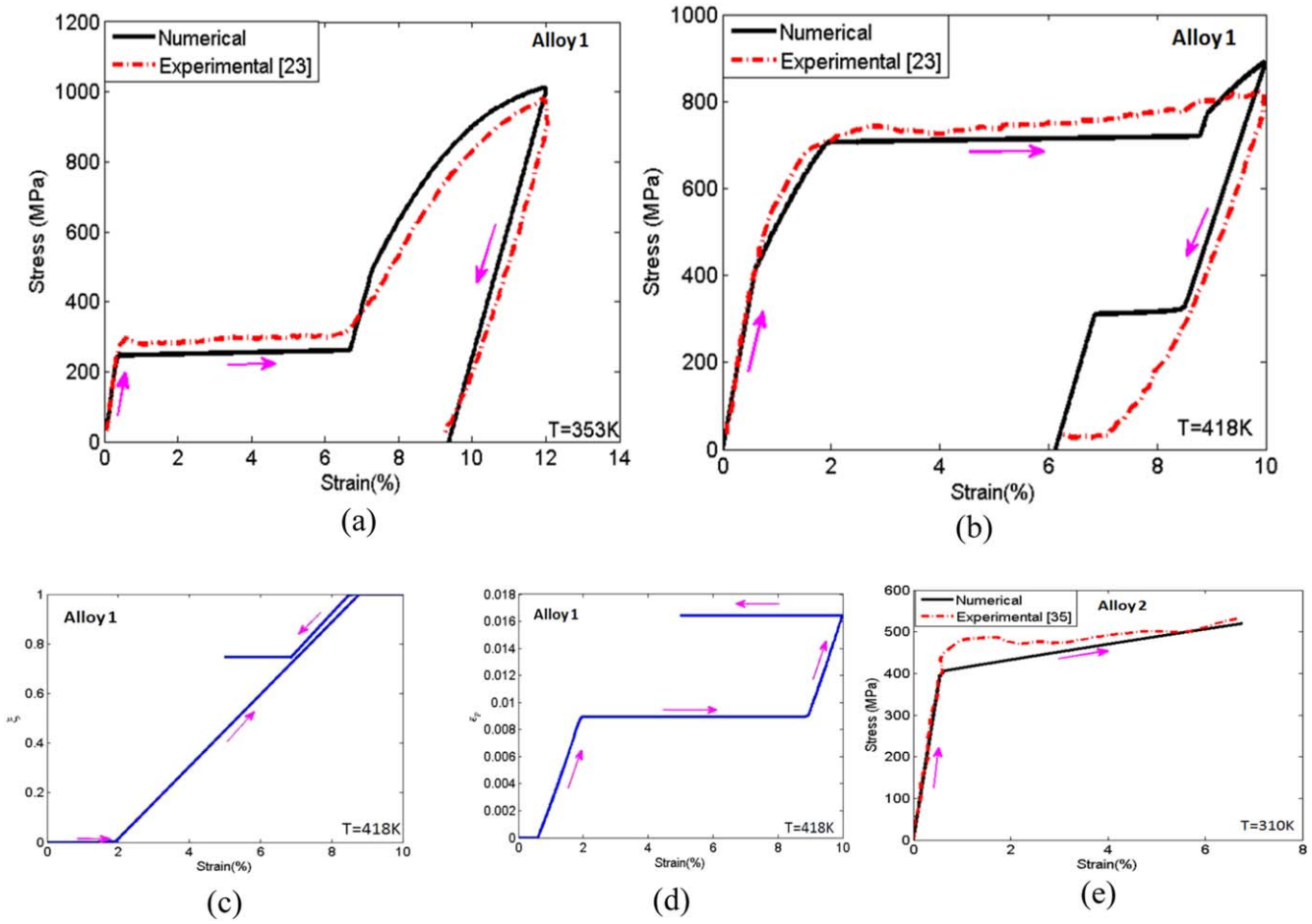

Figure 1. Tensile loading–unloading responses of Alloys 1 and 2. True stress–strain curve of Alloy 1, corresponding to (a) $T = 353$ K and (b) $T = 418$ K obtained from numerical simulations along with experimental data given in [23]. Evolution of (c) martensite volume fraction, and (d) equivalent plastic strain, $\bar{\epsilon}_p$ with strain for Alloy 1 at $T = 418$ K. (e) True stress–strain curve for Alloy 2 at $T = 310$ K obtained from numerical simulations along with experimental data given in [35].

problems have been obtained using 2D axisymmetric analysis). It is assumed that the contact between the specimen and the indenter is frictionless. The ratios of the radius and height of the specimen to the radius, R, of the indenter are both taken as 30. This is in accordance with studies which show that boundary effects do not influence stress distribution near the indented region as long as these ratios are greater than 10 [38]. Further, it is ensured that the extent of the transformed zone as well as that undergoing plastic deformation is well contained within the boundaries of the specimen.

The FE mesh used in the indentation analyses is comprised of four-noded isoparametric quadrilateral elements based on B-bar formulation [39, 40], which are gradually refined from the outer boundary of the specimen towards the indented zone. In figure 2, an enlarged view of the region near the indented zone is presented where elements of uniform size of about $0.01R$ have been employed. This mesh has been designed so as to accurately resolve the steep gradients in contact stress distribution and also to provide reliable estimates of the contact radius.

The spherical indenter is represented as a rigid surface (see figure 2). Contact between the indenter and the specimen is modeled using triangular gap elements. The stiffness matrix

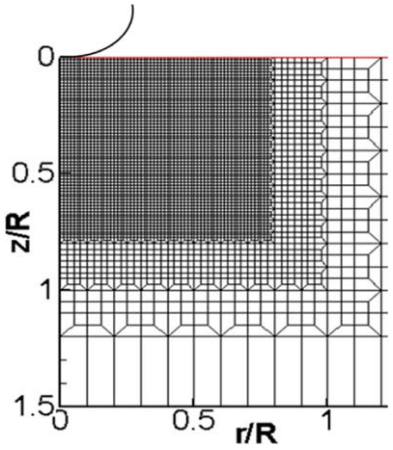

Figure 2. Enlarged view of the axisymmetric finite element mesh comprised of four-noded quadrilateral elements based on B-bar formulation used near the contact region between the rigid spherical indenter and cylindrical SMA specimen.

and force vector corresponding to these elements are derived based on a penalty formulation that treats their constitutive response as nonlinear elastic and penalizes penetration of the contacting surfaces into each other [37]. Since continuum

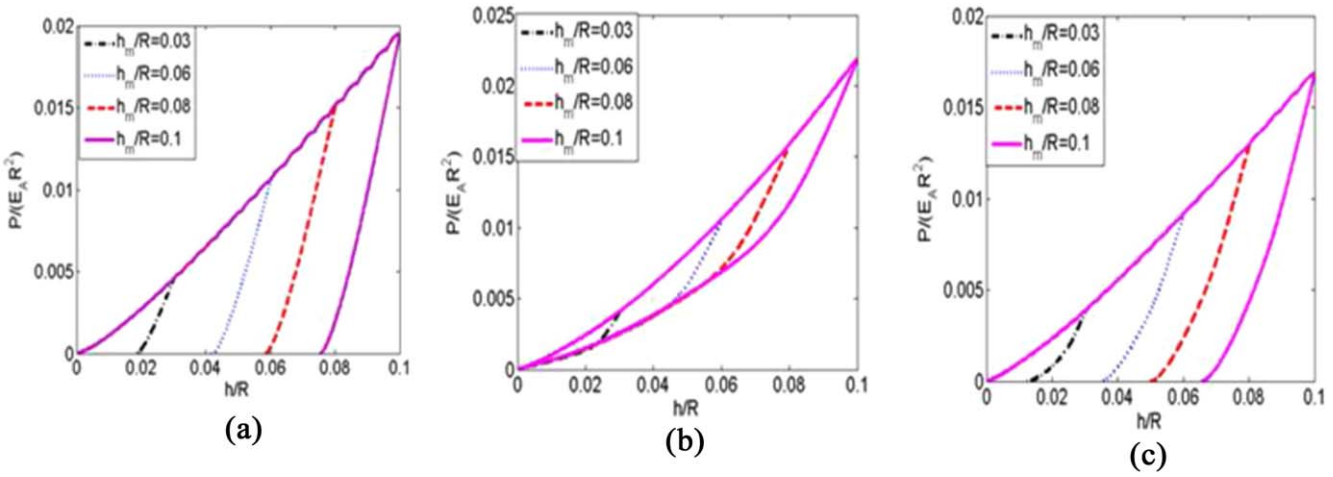

Figure 3. Normalized load-depth variations pertaining to Alloy 1 for (a) EPA, (b) SE and (c) SEP samples showing loading and unloading curves corresponding to different maximum indentation depths, h_m.

analyses with homogeneous material properties are conducted, the results obtained will depend only on the ratios of different length dimensions and not on their absolute values. Based on the analytical solution for contact between a rigid sphere and an elastic half-space as well as from dimensional considerations [41], it may be expected that the load, P, during indentation of a SMA will have the following functional form:

$$P = E_A R^2 f\left(\frac{h}{R}, \frac{E_A}{E_M}, \frac{Y_0^A}{E_A}, \text{ other material constants}\right). \quad (19)$$

In view of the above, the results will be presented in a suitably normalized form. Most of the results discussed are based on FE simulations with material constants pertaining to Alloy 1. A few important results of FE simulations with material parameters pertaining to Alloy 2 are also presented to further validate the proposed formulation and to establish the generic nature of the trends observed for Alloy 1.

4. Results and discussion

Indentation loading/unloading analyses for all the three material models considered, EPA, SE and SEP are performed up to maximum normalized depths (h_m/R) ranging from 0.01 to 0.1. For all the three cases, the initial phase present in the specimen is taken to be 100% austenite. The load-depth response, evolution of martensite volume fraction and plastic strain and the contact stress distribution pertaining to the three specimens are studied and compared against each other below.

4.1. Load versus indentation depth response

4.1.1. Loading behavior. The variation of normalized load, $P/(E_A R^2)$ with normalized indentation depth, h/R, pertaining to Alloy 1 for the three material models are plotted in figures 3(a)–(c). In each of these subfigures, loading and unloading responses corresponding to h_m/R of 0.03, 0.06, 0.08 and 0.1 are shown. It is observed that for small h/R, all three samples exhibit highly nonlinear load-depth response. On the other hand, as h/R increases, the normalized P–h curves corresponding to EPA and SEP samples tend to become linear, whereas that pertaining to SE specimen continues to remain strongly nonlinear. This can be clearly visualized from figures 4(a) and (b) where the normalized P–h curves for all three samples pertaining to Alloys 1 and 2, respectively, are directly compared up to $h_m/R = 0.1$. In order to quantify the above behavior, the following form:

$$\frac{P}{(E_A R^2)} = A\left(\frac{h}{R}\right)^n \quad (20)$$

is fitted to different portions of the P–h curves shown in figure 4(a). The values of exponent n, thus extracted are summarized in table 2 for Alloy 1. It can be seen from this table, that for small h/R (<0.0025), the value of n is about 1.42 for all three specimens, which is close to that predicted by the Hertz solution for contact of two elastic spheres ($n = 1.5$). As h/R increases, the value of n decreases progressively for EPA and SEP samples and is around 1.2 for h/R in the range of 0.05–0.08. This softening response is caused by stress relaxation in the progressively developing plastic zone around the contact region. Indeed, analytical (slip-line) solutions for wedge indentation of rigid perfectly plastic solids [41] indicate that $P \sim h$ (or $n \sim 1$). In contrast to the above, the n value for the SE specimen is also around 1.4 for small h/R and decreases to 1.25 in the range of h/R from 0.0025 to 0.025. This is attributed to stress relaxation arising from SE associated with phase transformation from austenite to martensite in the region around the zone of indentation (see section 4.2). However, unlike EPA and SEP samples, the exponent n for SE specimen enhances with further increase in indentation depth and attains a value of 1.41 for h/R in the range of 0.05–0.08. This stiffening behavior is caused by the elastic response of the material around the indenter after it transforms fully to martensite.

It can be observed from figure 4(a) that at low normalized load levels ($P/(E_A R^2) < 0.0025$) all the three specimens

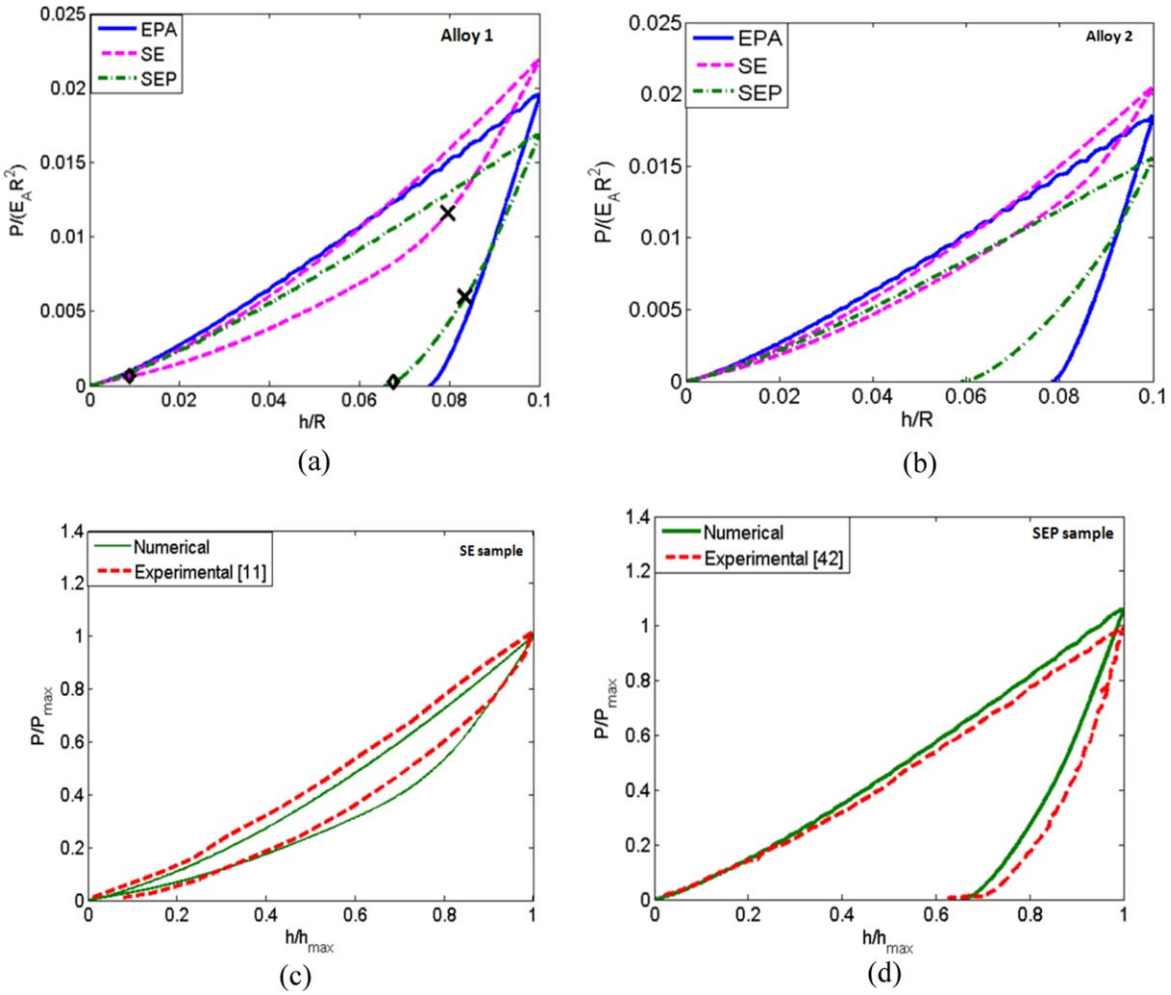

Figure 4. Comparison of the normalized load-depth responses for the three specimens indented up to maximum normalized depth of $h_m/R = 0.1$ followed by unloading for (a) Alloy 1 and (b) Alloy 2. The stages at which reverse transformation commences and ends for SE and SEP specimens are indicated by the 'x' and '◊' symbols on the respective unloading curves of Alloy 1. Comparison of normalized load-depth response of Alloy 1 corresponding to (c) SE specimen with experimental data given in [11] and (d) SEP sample with experimental data given in [42].

Table 2. Exponent n obtained by fitting equation of the form $P = Kh^n$ to various ranges of indentation depths for the three specimens pertaining to Alloy 1.

h/R	EPA specimen	SEP specimen	SE specimen
0–0.0025	1.43	1.42	1.42
0.0025–0.025	1.3	1.23	1.25
0.025–0.05	1.24	1.25	1.36
0.05–0.08	1.2	1.22	1.41

undergo almost the same level of deformation. This corresponds to the stage when the deformation for all three samples is primarily accommodated by the elastic response in the austenite phase. At intermediate load levels ($0.0025 < P/(E_A R^2) < 0.0125$), EPA experiences least deformation, followed by SE and then SEP specimens. This is because while the deformation in EPA specimen is accommodated primarily by elastic strains and to a smaller extent by plastic strains, in the SE sample they are accommodated by significant levels of transformation strains in addition to elastic strains. The SEP specimen shows maximum deformation because it can accumulate strain due to elastic, plastic and transformation processes.

At higher load levels ($P/(E_A R^2) > 0.0125$), SE specimen deforms the least, because now a large region underneath the indenter is already fully transformed into martensite and its ability to accommodate strains by phase transformation is exhausted. Thus, the deformation is largely sustained by elastic response of the martensite phase present in the transformed region beneath the indenter. The SEP sample displays maximum deformation, because it can still develop strains by elastic and plastic processes, now occurring predominantly in the transformed zone comprising of martensite phase. Also, at high $P/(E_A R^2)$, EPA deforms more than SE specimen as it can accommodate both elastic and plastic strains, but it deforms lesser than SEP sample because it is single phase austenite, which is stiffer than martensite. The same kind of comparative behavior can be observed for Alloy 2 which is austenitic at room temperature in figure 4(b). In order to understand how well the simulations

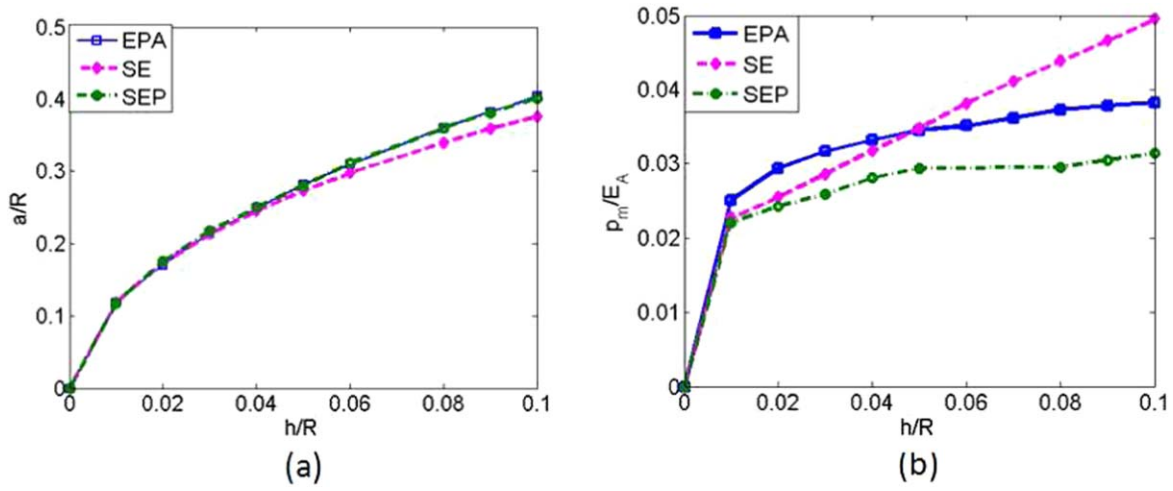

Figure 5. Variations of the (a) normalized contact radius, a/R, and (b) normalized mean contact pressure, p_m/E_A, with h/R for Alloy 1.

predict the qualitative nature of observed indentation behaviors, the load-depth variations of SE and SEP specimens pertaining to Alloy 1 are compared in normalized form (P/P_{max} versus h/h_{max}) with experimental data given in [11, 42], respectively, in figures 4(c) and (d). It can be observed that the normalized P–h curves obtained from simulations match reasonably well with the experimental variations. This validates the FE formulation further and also establishes that, in reality, the vastly different P–h responses corresponding to SE and SEP samples may both be exhibited by SMAs depending upon the relative values of the yield strengths and transformation stress as well as maximum load level P.

The normalized contact radius, a/R is plotted against h/R for all three specimens pertaining to Alloy 1 in figure 5(a). At a given h/R, a/R, which scales with the indentation strain [41] is about the same for SEP and EPA specimens but is somewhat higher compared to SE sample. This is due to plastic yielding which causes larger strains in the indented region. As already mentioned, plastic yielding underneath the indenter relaxes the stress levels which leads to lower mean contact pressure, p_m, for EPA and SEP specimens. This can be observed from the variations of p_m/E_A with h/R presented in figure 5(b). This figure shows that while for $h/R < 0.05$, p_m is slightly higher for EPA as compared to SE specimen due to marginally higher load (see figure 4(a)) it becomes markedly less than the latter for higher h/R. Also, the combination of stress relaxation due to SE and plasticity leads to pronounced decrease in p_m for SEP sample with respect to the other two specimens (see figure 5(b)).

4.1.2. Unloading behavior. On examining the unloading curves corresponding to different h_m/R shown in figure 3, it can be noted that EPA exhibits predominantly linear P–h response which indicates incrementally elastic behavior. By contrast, both SE and SEP specimens display an initially linear unloading P–h curve, followed by a nonlinear response. The stage at which the transition from linear to nonlinear unloading P–h response happens coincides with the onset of reverse transformation (martensite to austenite) in the indented zone and is marked by 'x' symbols on the unloading curves pertaining to SE and SEP specimens in figure 4(a). This identification is based on plots of effective martensite volume fraction versus h/R to be presented later. Further, the stage at which reverse transformation ends is also deduced from evolution of effective martensite volume fraction and indicated by a '◊' symbol on the unloading curves shown in figure 4(a). Interestingly, reverse transformation ends close to complete removal of load for both SE and SEP specimens.

Figure 3(b) shows that since the SE sample experiences complete reverse transformation, there is no residual indentation depth after unloading irrespective of h_m/R. On the other hand, for the SEP specimen, the reverse transformation is only partial, as will be seen subsequently, which leads to some residual indentation depth after load removal, even for small h_m/R (refer figure 3(c)). The total depth recovered upon unloading can be divided into an elastic part h_r^e and superelastic part h_r^{se} by extrapolating the initial linear portion of the unloading curve to zero load as indicated schematically in figure 6. In figure 7(a), the ratio h_r/h_m is plotted against h_m/R, where h_m is the maximum indentation depth (prior to the commencement of unloading) and $h_r = h_m - h_{res}$ is the recovered depth (refer figure 6) for EPA and SEP samples of Alloy 1. It can be seen from this figure, that, irrespective of h_m/R the depth recovered is higher for SEP specimen as compared to the EPA sample. This is because the SEP specimen experiences depth recovery due to both the superelastic and elastic processes. The superelastic depth recovery ratio, h_r^{se}/h_m for the SE and SEP specimens of Alloy 1 is plotted against h_m/R in figure 7(b).

From this figure, it is seen that the ratio $h_r^{se}/h_m \sim 0.6$ for the SE sample over a wide range of h_m/R while for the SEP specimen this ratio initially increases, attains a peak value at $h_m/R = 0.03$ and then starts decreasing. The reason for this contrasting trend is that while complete depth recovery takes place for the SE sample, the depth recovery for the SEP specimen is only partial due to development of plastic

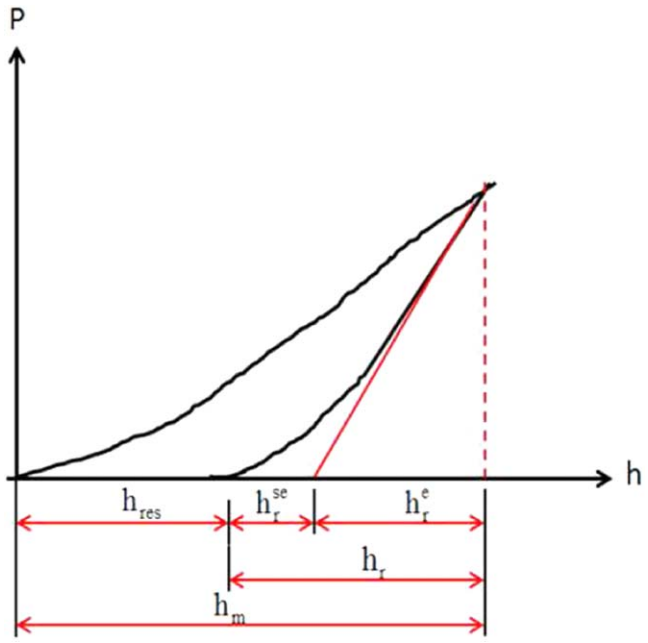

Figure 6. Schematic illustrating how the elastic depth recovered h_r^e and superelastic depth recovered h_r^{se} are calculated from the load-depth variation. Note: h_{res} is the residual (unrecovered) indentation depth upon complete unloading.

yielding. Further, as will be seen later, concurrent plastic yielding inhibits reverse transformation during unloading leading to even lower h_r^{se}/h_m values for SEP as compared to SE specimens as h_m/R increases.

The normalized slope of the initial, linear portion of the unloading curves shown in figure 3, $1/(E_A R)dP/dh$ is plotted against h_m/R in figure 7(C) for the three specimens considered. It can be seen from this figure, that for small h_m/R, the unloading slope is same for all three specimens since it is governed by the elastic modulus of the austenite phase. As h_m/R increases, the unloading slope for SE and SEP samples fall below that pertaining to EPA. This is an outcome of the phase transformation from austenite to martensite in the region below the indenter and the lower elastic modulus of the latter (refer table 1). Also, dP/dh at a given h_m/R is lower for SE as compared to the SEP specimen because, as will be seen later, the spatial extent of the transformed region is more for the former. Thus, the effective elastic modulus of the sample is less for the SE sample because of higher volume of martensite.

4.2. Spatial distribution and evolution of martensite volume fraction

The contours of martensite volume fraction, ξ, for SE and SEP specimens of Alloy 1 after indenting up to $h/R = 0.02$ are presented in figures 8(a) and (b), respectively. The ξ contours corresponding to $h/R = 0.05$ for the same specimens are displayed in figures 8(c) and (d) while similar contours for Alloy 2 at $h/R = 0.08$ are presented in figures 8(e) and (f). In this and other contour plots to be presented subsequently, the co-ordinate axes r and z are normalized by the contact radius, a. It can be seen from figures 8(a) and (b) that at small h/R, peak martensite volume fraction is attained at a certain depth below the surface along the indenter axis ($r = 0$) and also at the edge of contact ($r \to a$). This is because the maximum value of the Von Mises equivalent stress $\bar{\tau}$, which in the present constitutive model is assumed to drive the phase transformation (see equation (17)), occurs at these locations. At higher h/R level of 0.05, it can be seen from figures 8(c) and (d), that the region beneath the indenter is comprised of fully transformed martensite in the case of both SE and SEP samples. Also on comparing figures 8(a) with (b) and figures 8(c) with (d) it can be noted that irrespective of h/R, the size of the region undergoing phase transformation is larger for SE sample. A similar trend is noticed on comparing the ξ contours pertaining to SE and SEP samples of Alloy 2 (figures 8(e) and (f)) as well. In other words, at a given h/R, the extent of the transformed zone is diminished by the presence of concurrent plastic yielding. This can be clearly understood by examining figure 9 which shows plots of normalized height of fully transformed martensite zone measured along the indenter axis (i.e. at $r = 0$), H_t/R, versus h/R for Alloy 1. It can be seen that H_t for SE specimen becomes progressively higher compared to SEP sample as h/R increases. For example at $h/R = 0.1$, H_t is $0.65R$ and $0.48R$ for SE and SEP specimens, respectively. This is because plastic yielding relaxes the stress levels in the region underneath the indenter and therefore reduces the driving force for austenite to martensite phase transformation (see equations (17), (18)).

The effective martensite volume fraction, $\bar{\xi}$, is defined with respect to the volume of a cylindrical portion of the specimen underneath the indenter having radius R which is expected to participate predominantly in the deformation as:

$$\bar{\xi} = \frac{1}{(\pi R^2 H)} \int_V \xi dV, \tag{21}$$

where H is the height of the sample. The evolution of $\bar{\xi}$ with h/R during loading up to different h_m/R followed by unloading are shown in figures 10(a) and (b) for SE and SEP materials, respectively, of Alloy 1. It can be observed from figures 10(a) and (b) that following loading up to a given h/R, $\bar{\xi}$ is higher for SE than SEP specimen (as mentioned earlier). In order to visualize this clearly, evolution histories of $\bar{\xi}$ corresponding to $h_m/R = 0.1$ for the two samples are directly compared in figure 10(c). Thus, it can be seen from this figure that at $h/R = 0.1$, $\bar{\xi} = 0.0063$ and 0.0042 for SE and SEP specimens, respectively.

Upon unloading at a given h_m/R, it can be observed that, initially $\bar{\xi}$ remains almost constant while h decreases. In order to gain further insights on the above behavior, contour plots of ξ for the SE specimen of Alloy 1 after indenting up to a maximum normalized depth $h_m/R = 0.1$ (normalized load, $P/(E_A R^2) = 0.022$) and after unloading from this stage to $h_m/R = 0.08$ (normalized load, $P/(E_A R^2) = 0.012$) are presented in figures 11(a) and (b), respectively. These figures show that there is hardly any change in the spatial distribution of ξ between these two stages and hence this regime is termed as purely elastic recovery. On further unloading, $\bar{\xi}$ for the SE sample starts decreasing rapidly (see figure 10(c)) which

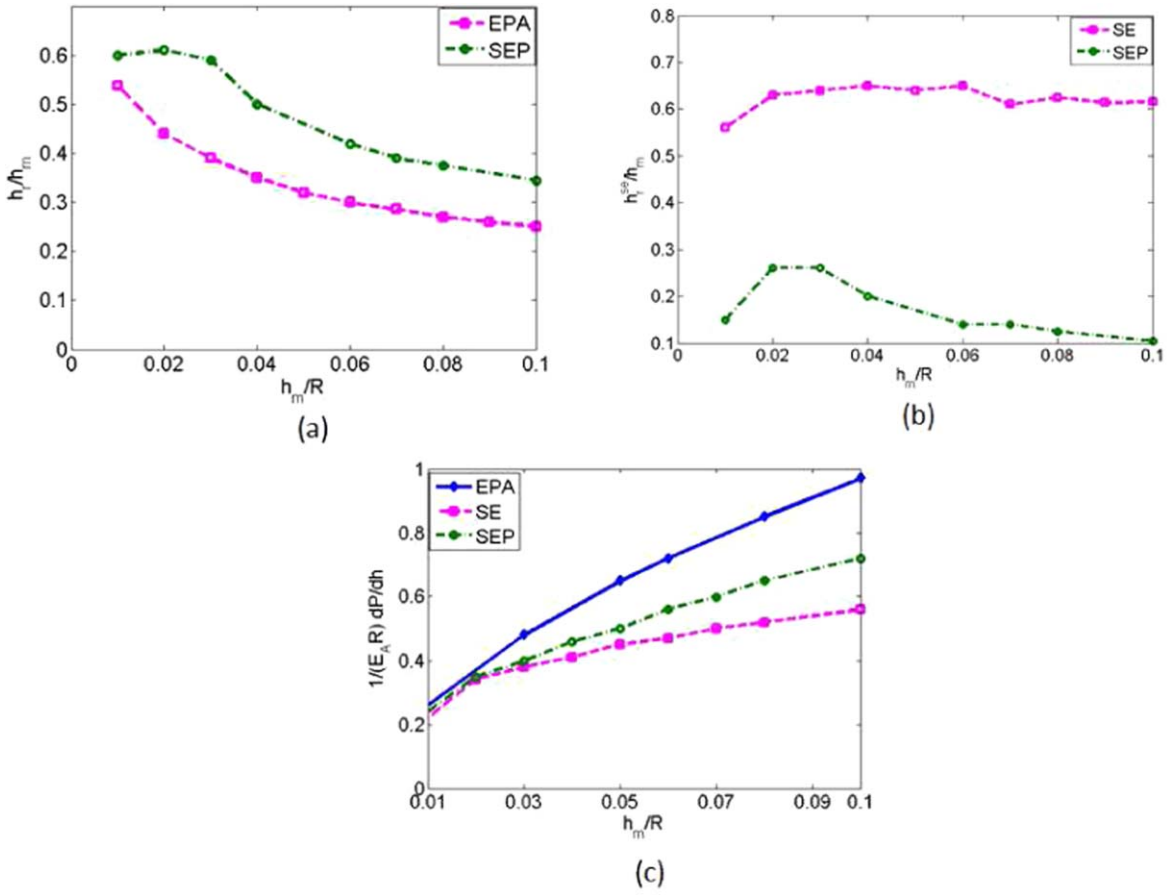

Figure 7. Comparison of (a) total depth recovery ratio, h_r/h_m versus h_m/R for EPA and SEP specimens, (b) superelastic depth recovery ratio h_r^{se}/h_m versus h_m/R for SE and SEP specimens on indenting up to and unloading from different h_m/R levels and (c) variation of the normalized slope of the initial unloading segment of the P–h curve with h_m/R for EPA, SE and SEP specimens. All plots pertain to Alloy 1.

signifies the onset of reverse transformation. The stage, thus identified, is marked by 'x' symbol in figure 10(c) as well as in the load-indentation depth curves presented earlier in figure 4(a). From figure 10(c), it can be seen that $\bar{\xi}$ and h decrease to zero at the end of unloading for SE sample which indicates complete reverse transformation and depth recovery. This can be observed from figure 11(c) which shows that there is no residual martensite following complete unloading ($P = 0$). The SEP sample also displays an initial regime of purely elastic recovery upon unloading, where $\bar{\xi}$ remains constant (see figure 10(b)). However, although $\bar{\xi}$ begins to drop with further unloading, it does not reduce to zero, but saturates at some level. The presence of a large zone of residual martensite can be perceived by examining figures 11(d) and (e), where contours of ξ for SEP sample corresponding to a maximum normalized indentation depth $h_m/R = 0.1$ (normalized load, $P/(E_A R^2) = 0.016$) and at end of complete unloading ($P = 0$) are presented. This is attributed to concurrent plastic deformation in the SEP specimen which sets a lower bound ξ_{lc} to the martensite volume fraction ξ during reverse transformation (see equation (20)). The ξ_{lc} contours at $h_m/R = 0.1$ are presented in figure 11(f). On examining figures 11(d) and (e) along with the above figure, it can be noticed that reverse transformation has occurred only in regions where $\xi > \xi_{lc}$ at peak load. The stage at which the reverse transformation ceases is identified as the load level during unloading at which the slope of the $\bar{\xi}$ versus h/R curve drops to 10% of that at end of forward transformation ($P = P_{max}$). This stage has been marked by '◊' symbols in the unloading segments shown in figures 10(c) and 4(a). The onset of reverse transformation during unloading, as deduced from the plots shown in figure 10(c), can be distinctly identified from the P–h variation (see figure 4(a)) as the stage at which the initial linear portion of the unloading segment starts deviating from linearity. On the other hand, the end of reverse transformation does not show a perceptible change in the nature of the unloading segment. It can be noted, however that cessation of reverse transformation occurs very close to the completion of unloading and experimentalists can this can be considered in experimental studies as the stage at which reverse transformation ends. The above criteria will be useful in separating the contributions of elastic and reverse transformation processes to the total depth recovered and also help in deducing the Oliver–Pharr modulus with better accuracy [21].

4.3. Equivalent plastic strain distribution

The contours of equivalent plastic strain $\bar{\varepsilon}_p$ at $h_m/R = 0.05$ for EPA and SEP specimens of Alloy 1 are shown in

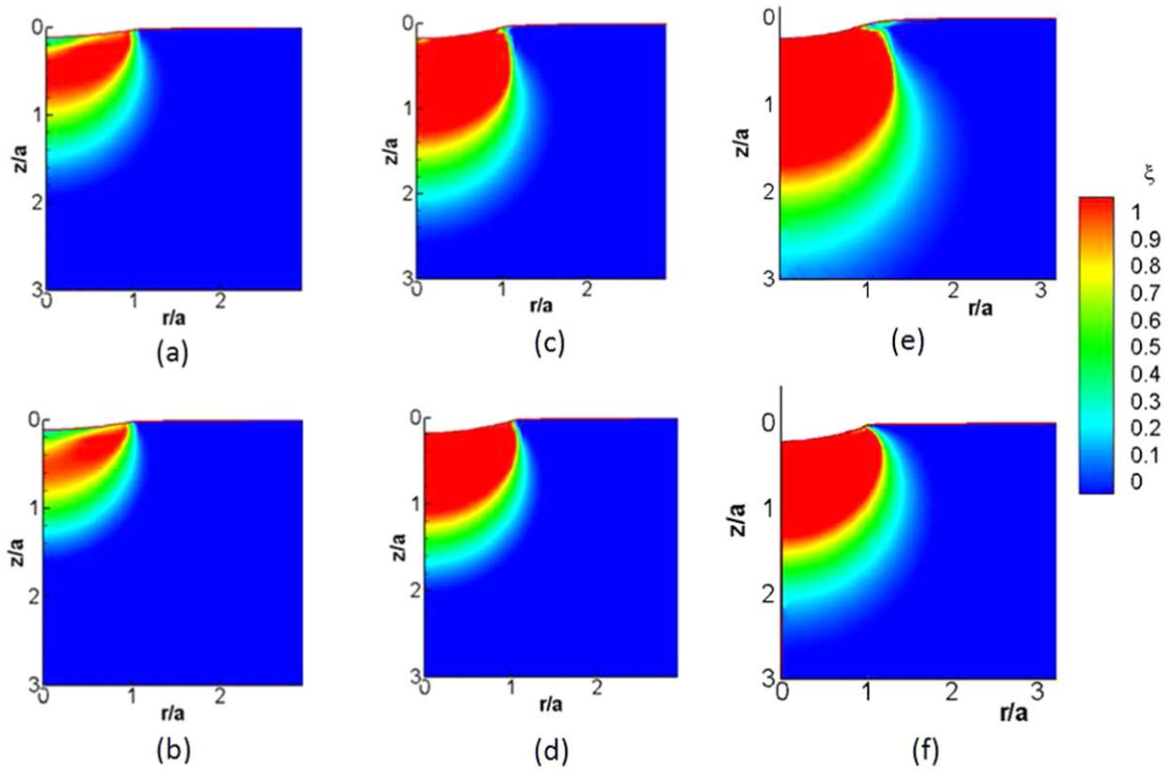

Figure 8. Martensite volume fraction contours for Alloy 1 corresponding to (a) SE specimen, at $h/R = 0.02$, (b) SEP sample, at $h/R = 0.02$, (c) SE specimen, at $h/R = 0.05$ and (d) SEP sample, at $h/R = 0.05$. Similar contours for Alloy 2 at $h/R = 0.08$ corresponding to (e) SE specimen and (f) SEP specimen.

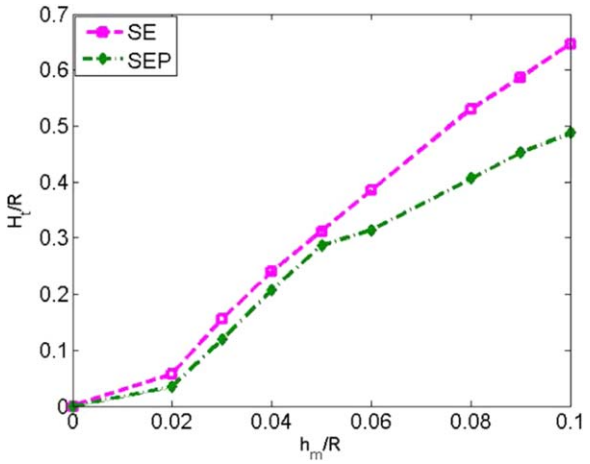

Figure 9. Variation of the size of the fully transformed martensite region along the indenter axis, $r = 0$, with h/R for Alloy 1.

figures 12(a) and (b), respectively, while similar plots are displayed in figures 12(c) and (d) for Alloy 2 at $h_m/R = 0.08$. The plastic strain levels are high at the edge of contact and at some depth below the specimen surface, which is akin to the martensite volume fraction contours at low indentation depth (see figures 8(a) and (b)) and is traced to the equivalent stress distribution. Also, on comparing figures 12(a) and (b) it can be observed that the level of $\bar{\varepsilon}_p$ as well as the spatial extent over which high $\bar{\varepsilon}_p$ prevails are larger for EPA specimen. Similar behavior can be observed for Alloy 2 from figures 12(c) and (d). Indeed, it can be seen from the variation of $\bar{\varepsilon}_p$ with z/a along the indenter axis ($r = 0$) shown in figures 13(a) and (b) that the evolution of $\bar{\varepsilon}_p$ with respect to h_m/R is faster for EPA. For example, corresponding to $h_m/R = 0.1$, the peak value of $\bar{\varepsilon}_p$ is 0.2 (at $z/a = 0.2$) for EPA, whereas it is 0.08 (at same z/a) for the SEP specimen. Also, the distance over which $\bar{\varepsilon}_p > 0.01$ for EPA is almost twice that for SEP sample. Thus, the coupling between plastic deformation and phase transformation causes mutual retardation in evolution of $\bar{\varepsilon}_p$ (noted from SEP versus EPA specimen response) and ξ (observed from SEP versus SE specimen response).

4.4. Stress distributions

The contours of normalized axial and shear stresses, σ_{zz}/E_A and τ_{rz}/E_A, at $h_m/R = 0.05$ for all the three specimens of Alloy 1 are displayed in figures 14(a)–(c) and (d)–(f), respectively. Figure 14(a) shows that magnitude of σ_{zz} is uniform over the contact zone for EPA, whereas it is high near the edge of contact for SE and SEP specimens (see figures 14(b) and (c)). It can be observed from figures 14(d)–(f) that τ_{rz} is high near the edge of contact for all three specimens. A comparison of the magnitudes of the axial and shear stresses for the three materials shows that they are highest for SE sample and lower for EPA and SEP samples, which is attributed to plastic yielding.

The radial variations of σ_{zz} and σ_{rr}, normalized by mean contact pressure p_m, on the specimen surface, for Alloy 1 at $h_m/R = 0.05$ are shown in figures 15(a) and (b), respectively.

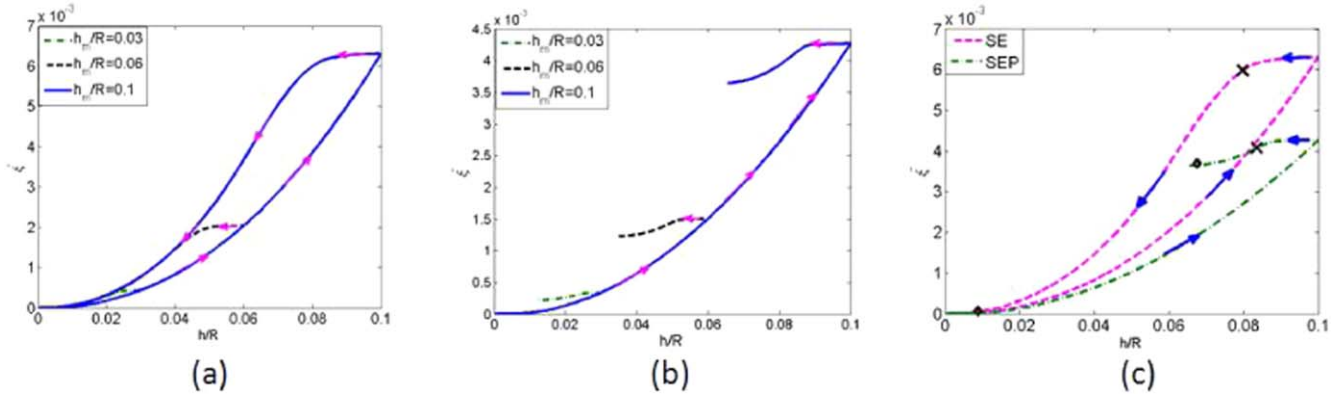

Figure 10. Variation of effective martensite volume fraction $\bar{\xi}$ with h/R for (a) SE and (b) SEP material showing loading and unloading segments corresponding to different maximum normalized depths h_m/R. (c) Comparison of variations of $\bar{\xi}$ with h/R for SE and SEP materials indented up to $h_m/R = 0.1$ followed by unloading. The stage at which reverse transformation commences and ends are marked by 'x' and '◇' symbols, respectively, on the unloading segments.

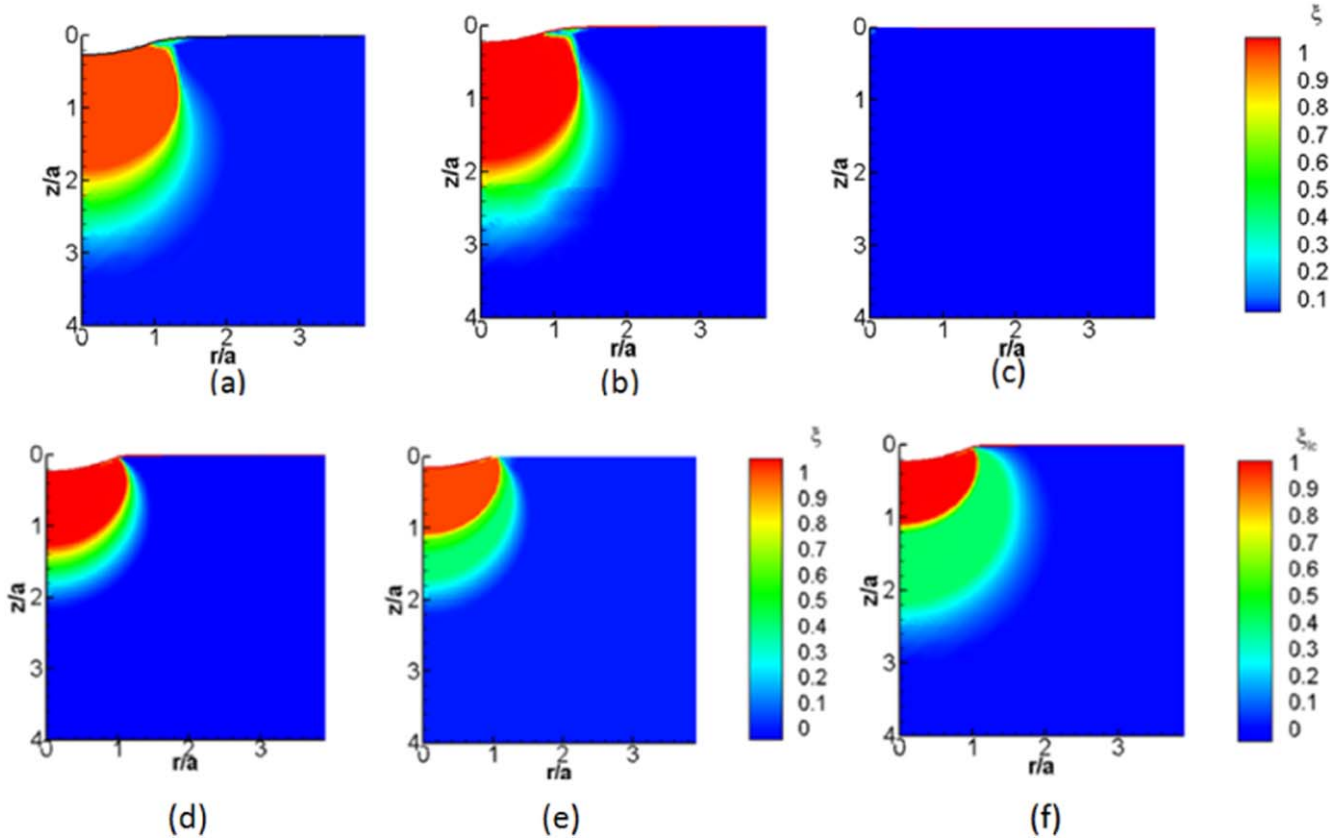

Figure 11. Martensite volume fraction contours for SE sample at various stages of unloading after indenting up to $h_m/R = 0.1$: (a) at peak load, $P/(E_A R^2) = 0.022$, (b) at an intermediate unloading stage, $P/(E_A R^2) = 0.012$ and (c) after complete unloading, $P = 0$. Martensite volume fraction contours for SEP sample: (d) after indenting up to $h_m/R = 0.1$ and (e) after complete unloading, $P = 0$. (f) Contour plot of lower bound to martensite volume fraction during unloading, ξ_{lc}, after indenting up to $h_m/R = 0.1$. All plots pertain to Alloy 1.

As observed from the contour plots, the magnitude of σ_{zz} is uniform on the surface over the entire contact zone for EPA, whereas it peaks close to the edge of contact for SE and SEP specimens (see figure 15(a)). This effect is quite pronounced for SE sample and is due to phase transformation occurring earlier in this region (see figure 8), which is mitigated to some extent by plastic yielding for the SEP sample. From figure 15(b), it can be observed that the distribution of σ_{rr} is quite uniform over the contact zone for the EPA and SEP specimens. On the other hand, for the SE sample, it reaches a compressive peak near the edge of contact similar to σ_{zz}. Also, a tensile peak in σ_{rr} just outside the contact zone may be perceived for this specimen, which is a characteristic feature of Hertz contact in elastic solids and can trigger brittle ring cracks [41]. In the presence of plasticity, this does not occur

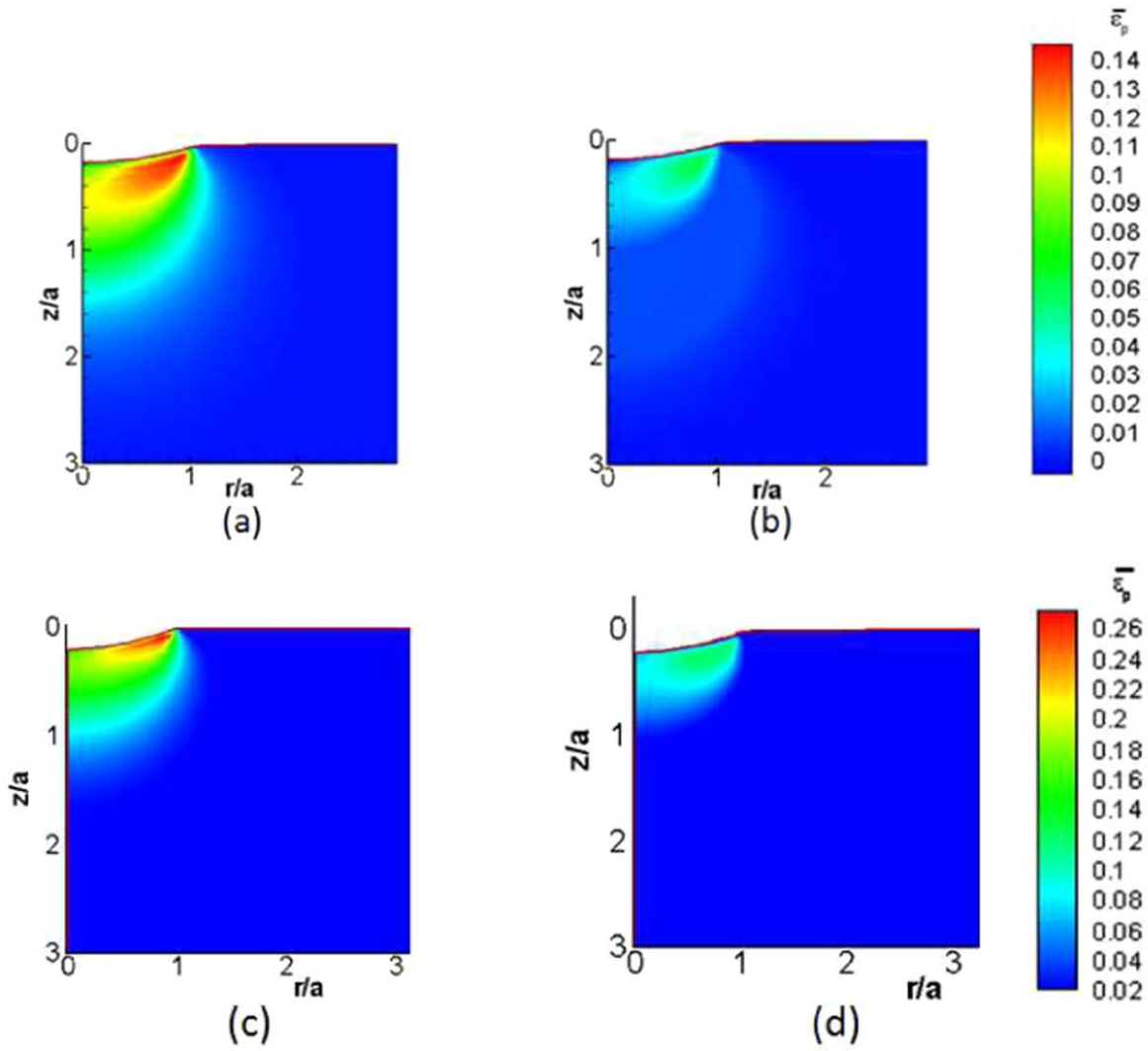

Figure 12. Equivalent plastic strain contours at $h_m/R = 0.05$ for (a) EPA and (b) SEP specimens of Alloy 1. Similar contours at $h_m/R = 0.08$ for (c) EPA and (d) SEP specimens of Alloy 2.

as can be seen from the σ_{rr} variations pertaining to EPA and SEP samples in figure 15(b).

In order to understand the subsurface stress distribution for SE and SEP specimens, which involves a complex interplay of phase transformation and plasticity effects, variations of σ_{zz}/p_m, σ_{rr}/p_m and normalized maximum shear stress, τ_{max}/p_m with z/R along the indenter axis ($r = 0$) at $h_m/R = 0.03$ for austenite sample of Alloy 1 exhibiting purely elastic behavior and elastic-plastic response are first presented in figures 16(a) and (b). For purely elastic response, $|\sigma_{zz}/p_m|$ decreases sharply from peak value of 1.5 at the specimen surface as z decreases (see figure 16(a)). The maximum shear stress τ_{max} attains a peak value of $0.5p_m$ at $z/a \sim 0.4$. By contrast, for EPA specimen, it can be seen from figure 16(b) that τ_{max} is constant at about $0.2p_m$ over the plastic zone which extends up to $z/a \sim 1.5$ and then decreases. The magnitude of normalized axial stress $|\sigma_{zz}/p_m|$ has a peak value of about 1 at $z = 0$. Both σ_{zz} and σ_{rr} decrease more gradually in magnitude with increase in subsurface depth as compared to the purely elastic case.

The subsurface normalized stress variation for SE specimen of Alloy 1 along $r = 0$ at $h_m/R = 0.01$ and 0.05 are shown in figures 16(c) and (d), respectively. Similar normalized stress variation plots for SEP specimen are displayed in figures 16(e) and (f). For the SE sample, at small h_m/R of 0.01, when phase transformation is taking place just below the indenter, the stress distributions are qualitatively similar to EPA (compare figures 16(c) with (b)). Thus $\tau_{max}/p_m \sim 0.2$ over the transforming region and $|\sigma_{zz}/p_m|$ decreases from a peak value of 1 as z increases. At higher h_m/R, it can be seen from figure 16(d) that $\tau_{\max}/p_m$ increases to a peak value at some depth below the surface in the fully transformed martensite region (refer figure 8(a)). This peak value is found to enhance with increase in h_m/R and approach the limiting value of 0.5 for purely elastic response (figure 16(a)). At higher depth, z/a, where the material is undergoing austenite to martensite phase transformation, τ_{max}/p_m is almost constant at around 0.2, whereas $|\sigma_{zz}/p_m|$ and $|\sigma_{rr}/p_m|$ decrease almost linearly with z (see figure 16(d)).

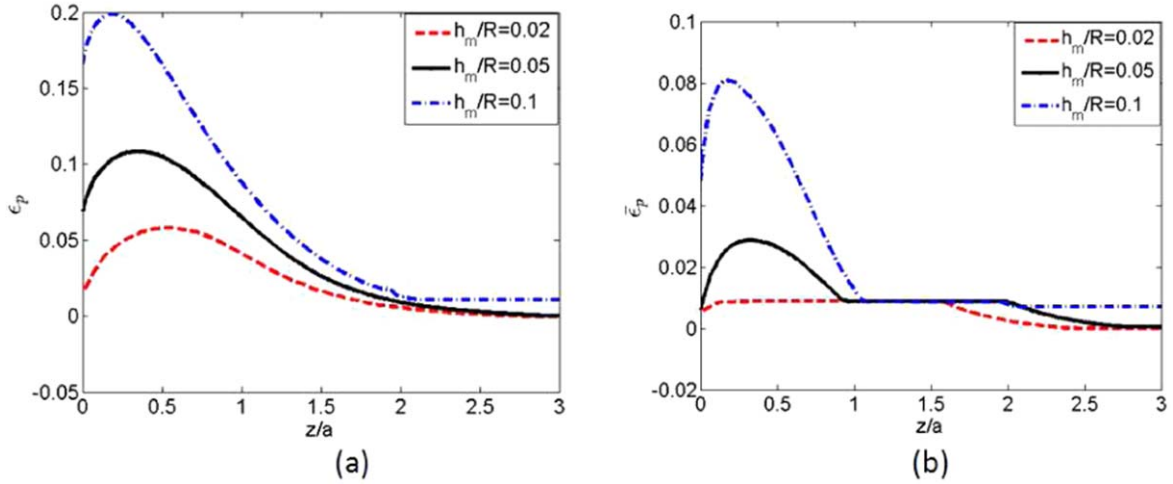

Figure 13. Variations of the equivalent plastic strain at different h_m/R along the indenter axis ($r = 0$) for (a) EPA and (b) SEP specimens of Alloy 1.

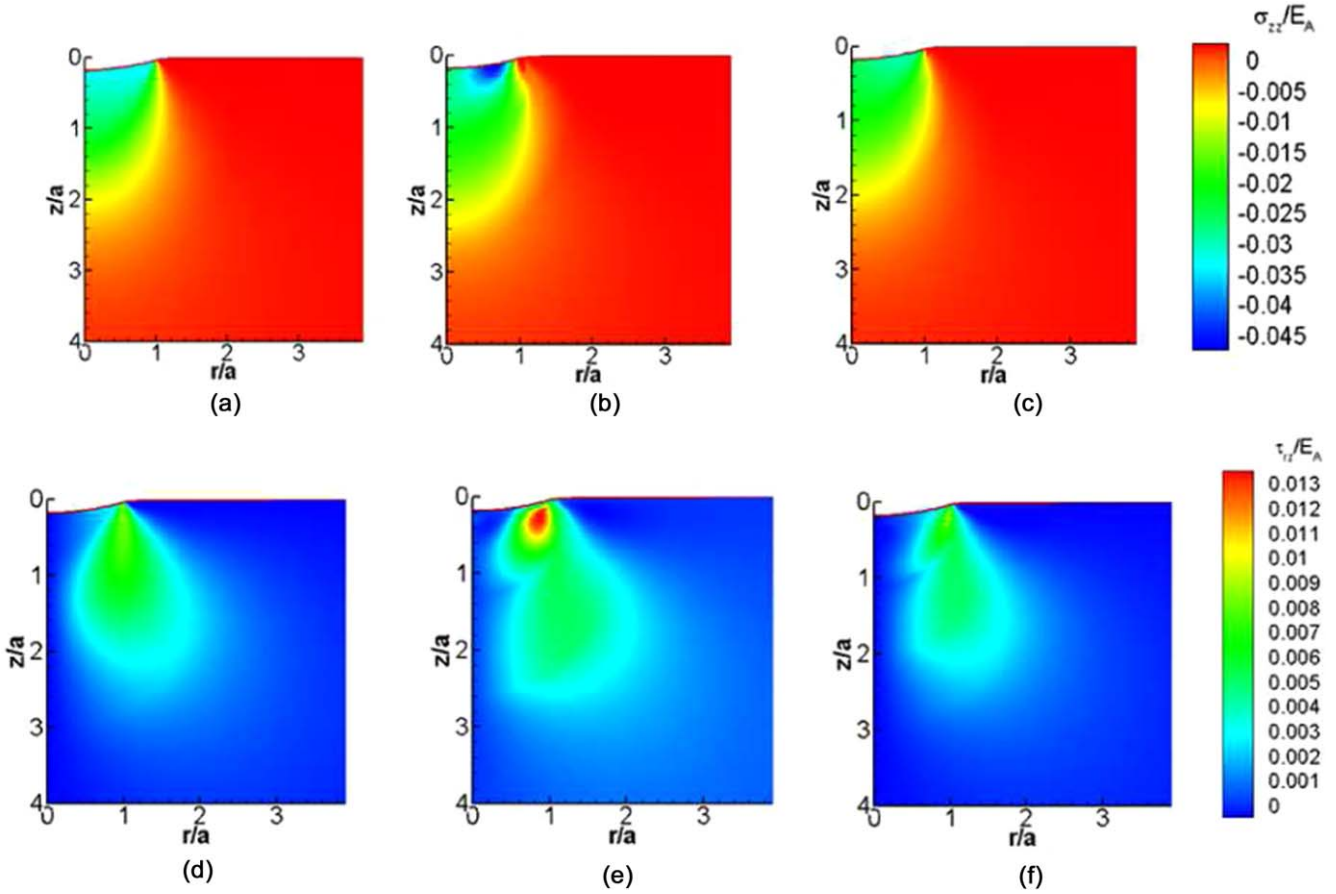

Figure 14. Contours of normalized axial stress, σ_{zz}/E_A, at $h_m/R = 0.05$ for (a) EPA, (b) SE and (c) SEP specimens of Alloy 1. Contours of normalized shear stress, τ_{rz}/E_A, at $h_m/R = 0.05$ for (d) EPA, (e) SE and (f) SEP specimens of Alloy 1.

In the case of SEP specimen, the subsurface stress variations along the indenter axis are similar to SE sample at small h_m/R (compare figures 16(c) and (e)). However, after complete transformation to martensite occurs below the indenter, plasticity influences the stress variations as can be seen from figure 16(f). Thus, $\tau_{max}/p_m \sim 0.2$ both within the fully transformed martensite (small z/a) as well as in the region undergoing phase transformation at higher depths below the surface. For example at $h_m/R = 0.05$, plastic deformation in the fully transformed martensite influences the stress variation upto $z/a \sim 1$, whereas the role of ongoing phase transformation affects the stress distribution between $z/a \sim 1$ to 2. Beyond $z/a = 2$, the stress variation is governed only by elastic response in the untransformed austenite phase.

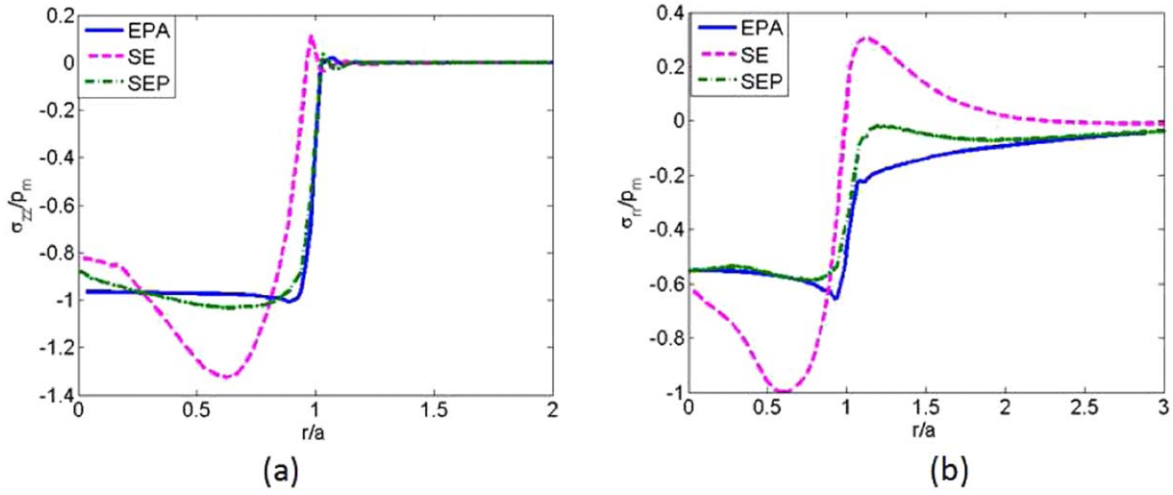

Figure 15. Variations of (a) normalized axial stress, σ_{zz}/p_m, and (b) normalized radial stress, σ_{rr}/p_m along the specimen surface for all three specimens of Alloy 1 at $h_m/R = 0.05$. Here, the stresses have been normalized by the mean contact pressure, p_m.

The above discussion shows that stress distribution in SMAs due to indentation reflects the role of plastic deformation in the fully transformed martensite at low subsurface depths and ongoing phase transformation (SE effect) at higher subsurface depths. It must be noted that the constitutive model used in this work assumes isotropic, homogeneous nature of the SMAs. While this accurately captures the macroscopic mechanical response of SMAs, it does not take into account microstructural features like texture, precipitates, etc and how these influence phase transformation and plastic yielding behavior. Also, there may be more than one variant of the stress-induced martensite phase formed which will induce anisotropy in the specimen considered. The axisymmetric modeling of the spherical indentation problem may no longer be valid under the above conditions. Thus, the results presented above are representative in a homogenized sense of an SMA system, initially in the austenite phase, that forms multiple variants of martensite phase on loading if the alloy is not sharply textured.

5. Summary and conclusions

The spherical indentation behavior of SMAs has been investigated using a constitutive model that is able to capture the coupled transformation-plasticity response. FE analyses have been conducted by considering SE without and with plastic deformation in the component phases (SE and SEP specimens), as well as a conventional elastic-plastic specimen having the properties of the austenite phase (EPA sample). The simulations have been performed for two Ni–Ti alloys with different A_f to establish the generic nature of the results. The following are the salient conclusions of this work.

- The P–h curves for all three specimens are close to each other during the initial stage of indentation and follow a variation of the form $P \sim h^n$, with $n \sim 1.4$, which is close to that predicted by the Hertz solution. With increase in indentation depth, n for EPA and SEP progressively decreases and appears to be tending to 1 at high h/R, which is characteristic of elastic-plastic material behavior [41]. On the other hand, for SE specimen, n first decreases with increase in h like in the other two specimens, but enhances to $\sim$1.4 at later stages. Also, at later stages of indentation, h at a given load is lowest for SE, followed by EPA and SEP specimens.
- While the predominant part of the P–h curve during unloading is linear for the EPA sample, an initial linear response, followed by a strong nonlinear variation is observed in the case of SE and SEP specimens. The stage at which the transition from linear to nonlinear behavior occurs coincides with commencement of reverse transformation in the indented material. At large h, slope of the unloading P–h response is highest for EPA sample, followed by SEP and SE specimens. This is an outcome of transformation from austenite to martensite phase in the SE and SEP specimens and the lower elastic modulus of martensite.
- During unloading, the indentation depth is fully recovered for the SE sample, whereas the other two specimens display residual indentation depths owing to plastic deformation and incomplete reverse transformation. The ratio of depth recovered due to SE to maximum indentation depth is fairly constant at about 0.6 for SE material, whereas it progressively reduces for SEP specimen.
- The spatial extent of the region of transformed martensite at a given h is lower for SEP compared to SE specimen. Further, the evolution of the effective martensite volume fraction $\bar{\xi}$ with respect to h is slower for this case and is only 2/3rd of that pertaining to SE sample at $h/R = 0.1$. This is caused by stress relaxation arising from plastic deformation which reduces the driving force for phase transformation.
- During initial stages of unloading, the transformed region as well as the effective martensite volume fraction do not

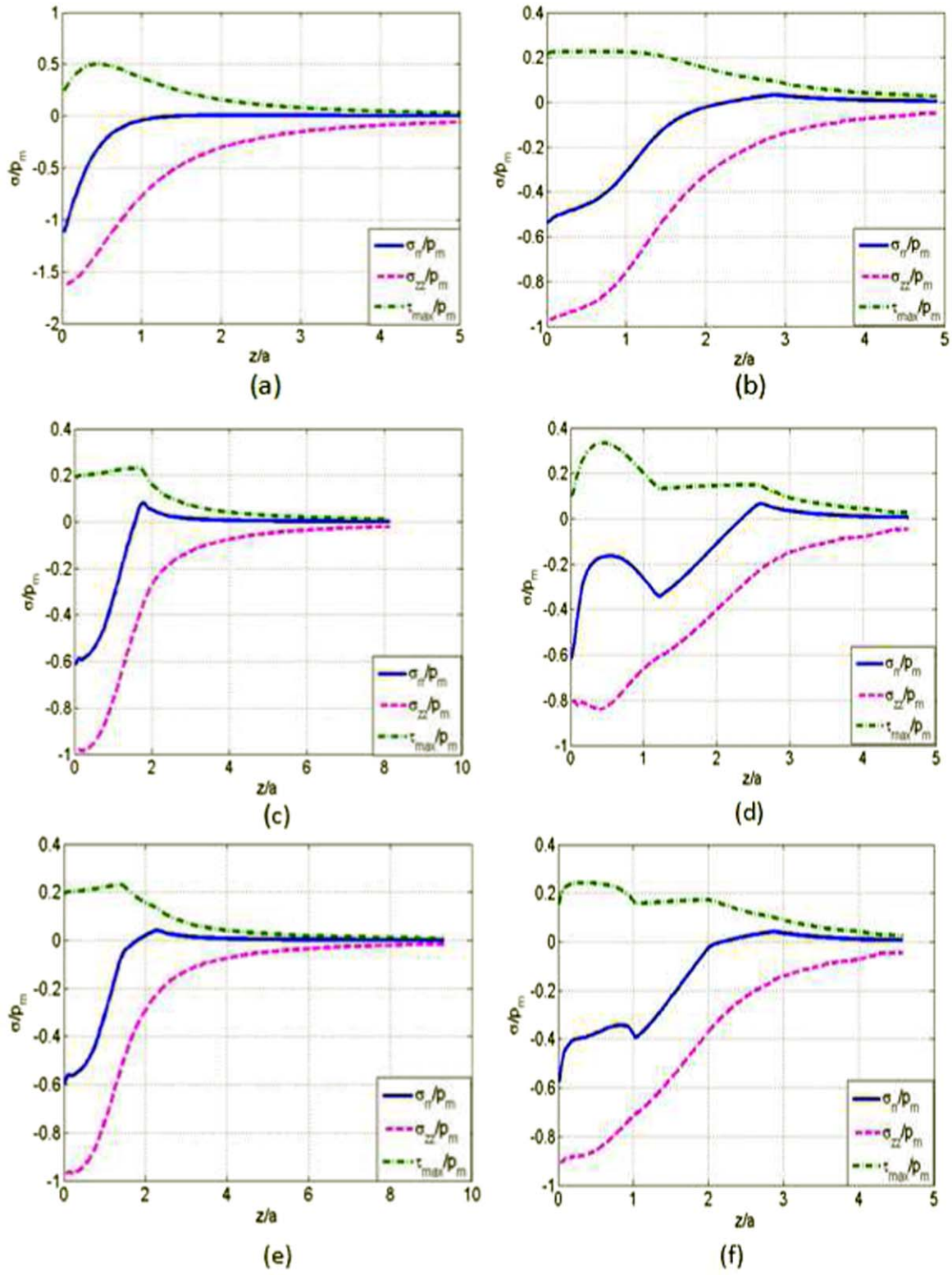

Figure 16. Variation of stresses normalized by mean contact pressure, σ/p_m, with z/a along indenter axis ($r = 0$) for (a) elastic and (b) EPA specimens at $h_m/R = 0.03$. Similar variations for SE specimen at (c) $h_m/R = 0.01$ and (d) $h_m/R = 0.05$ and for SEP specimen at (e) $h_m/R = 0.01$ and (f) $h_m/R = 0.05$. All plots pertain to Alloy 1.

change. However, with further reduction in load, reverse transformation takes place leading to drop in $\bar{\xi}$ and recovery in indentation depth which are total in the case of SE specimen and partial for the SEP sample. Indeed, $\bar{\xi}$ saturates after decreasing for the latter signifying end of reverse transformation.

- The coupling between phase transformation and plastic yielding retards the latter, in the sense that the level of

plastic strain as well as the spatial extent of region experiencing high plastic strains at a given h are lower for the SEP sample compared to the EPA specimen.

- The magnitude of axial stress σ_{zz} and shear stress τ_{rz} in the region just below the indenter are diminished by presence of plastic yielding. Also, while σ_{zz} distribution over the contact zone is uniform for the EPA specimen, it peaks in magnitude close to the edge of contact for SE and SEP samples and is attributed to phase transformation occurring earlier in this region. A similar behavior is noticed in variation of σ_{rr} for SE sample, with the additional feature of a strong tensile peak just outside the edge of contact.
- A complex interplay of phase transformation and plasticity effects is observed in the subsurface stress distribution. Thus, for the SE specimen, the maximum normalized shear stress $\tau_{max}/p_m \sim 0.2$ at subsurface depths where phase transformation is taking place. It increases after phase transformation is completed. By contrast, for the SEP specimen, $\tau_{max}/p_m \sim 0.2$ both at small subsurface depths where martensite has fully formed and at larger depths below the indenter where phase transformation is ongoing.

Acknowledgments

R Narasimhan would like to gratefully acknowledge the Science and Engineering Research Board (Government of India) for financial support under the JC Bose Fellowship scheme.

ORCID iDs

R Narasimhan https://orcid.org/0000-0003-3655-450X

References

[1] Duerig T W, Melton K and Stöckel D 2013 *Engineering Aspects of Shape Memory Alloys* (London: Butterworth-Heinemann)
[2] Otsuka K and Wayman C M 1999 *Shape Memory Materials* (Cambridge: Cambridge University Press)
[3] Otsuka K and Ren X 2005 Physical metallurgy of Ti–Ni-based shape memory alloys *Prog. Mater. Sci.* **50** 511–678
[4] Humbeeck J Van 1999 Non-medical applications of shape memory alloys *Mater. Sci. Eng.* A **273** 134–48
[5] Duerig T, Pelton A and Stöckel D 1999 An overview of nitinol medical applications *Mater. Sci. Eng.* A **273** 149–60
[6] Machado L and Savi M 2003 Medical applications of shape memory alloys *Braz. J. Med. Biol. Res.* **36** 683–91
[7] Fu Y, Du H, Huang W, Zhang S and Hu M 2004 TiNi-based thin films in mems applications: a review *Sensors Actuators* A **112** 395–408
[8] Oliver W C and Pharr G M 1992 An improved technique for determining hardness and elastic modulus using load and displacement sensing indentation experiments *J. Mater. Res.* **7** 1564–83
[9] Gall K, Dunn M L, Liu Y, Labossiere P, Sehitoglu H and Chumlyakov Y I 2002 Micro and macro deformation of single crystal NiTi *J. Eng. Mater. Technol.* **124** 238–45
[10] Gall K, Juntunen K, Maier H, Sehitoglu H and Chumlyakov Y I 2001 Instrumented micro-indentation of NiTi shape-memory alloys *Acta Mater.* **49** 3205–17
[11] Ni W, Cheng Y-T and Grummon D S 2004 Microscopic shape memory and superelastic effects under complex loading conditions *Surf. Coat. Technol.* **177** 512–7
[12] Li P, Karaca H E and Cheng Y-T 2015 Spherical indentation of NiTi-based shape memory alloys *J. Alloys Compd.* **651** 724–30
[13] Ma X-G and Komvopoulos K 2003 Nanoscale pseudoelastic behavior of indented titanium–nickel films *Appl. Phys. Lett.* **83** 3773–5
[14] Wood A M and Clyne T 2006 Measurement and modelling of the nanoindentation response of shape memory alloys *Acta Mater.* **54** 5607–15
[15] Yan W, Sun Q, Feng X-Q and Qian L 2006 Determination of transformation stresses of shape memory alloy thin films: a method based on spherical indentation *Appl. Phys. Lett.* **88** 241912
[16] Qian L, Zhang S, Li D and Zhou Z 2009 Spherical indentation for determining the phase transition properties of shape memory alloys *J. Mater. Res.* **24** 1082–6
[17] Gan B, Gatepin M, Cantonwine S and Tin S 2012 *In situ* characterization of the martensitic transformation temperature of NiTi shape memory alloys via instrumented microindentation *Phil. Mag. Lett.* **92** 254–61
[18] Yan W, Sun Q, Feng X-Q and Qian L 2007 Analysis of spherical indentation of superelastic shape memory alloys *Int. J. Solids Struct.* **44** 1–17
[19] Zhang Y, Cheng Y-T and Grummon D S 2007 Finite element modeling of indentation-induced superelastic effect using a three-dimensional constitutive model for shape memory materials with plasticity *J. Appl. Phys.* **101** 053507
[20] Shastry V V and Ramamurty U 2013 Temperature dependence of indentation recovery ratios in austenitic and martensitic shape memory alloys *Smart Mater. Struct.* **22** 077002
[21] Kan Q, Yan W, Kang G and Sun Q 2013 Oliver–Pharr indentation method in determining elastic moduli of shape memory alloys phase transformable material *J. Mech. Phys. Solids* **61** 2015–33
[22] Ahlers M 2007 Martensitic transformation and plastic deformation: a comparison *Smart Mater. Struct.* **16** S115
[23] Hartl D and Lagoudas D 2009 Constitutive modeling and structural analysis considering simultaneous phase transformation and plastic yield in shape memory alloys *Smart Mater. Struct.* **18** 104017
[24] Giannakopoulos A, Larsson P-L and Vestergaard R 1994 Analysis of vickers indentation *Int. J. Solids Struct.* **31** 2679–708
[25] Larsson P-L, Giannakopoulos A, Söderlund E, Rowcliffe D and Vestergaard R 1996 Analysis of Berkovich indentation *Int. J. Solids Struct.* **33** 221–48
[26] Simo J C and Hughes T J 2006 *Computational Inelasticity* vol 7 (New York: Springer)
[27] Lagoudas D, Hartl D, Chemisky Y, Machado L and Popov P 2012 Constitutive model for the numerical analysis of phase transformation in polycrystalline shape memory alloys *Int. J. Plast.* **32** 155–83
[28] Lagoudas D C 2008 *Shape Memory Alloys: Modeling and Engineering Applications* (New York: Springer)
[29] Nemat-Nasser S and Choi J Y 2005 Strain rate dependence of deformation mechanisms in a Ni–Ti–Cr shape-memory alloy *Acta Mater.* **53** 449–54
[30] Nemat-Nasser S, Choi J Y, Guo W-G, Isaacs J B and Taya M 2005 High strain-rate, small strain response of a NiTi shape-memory alloy *J. Eng. Mater. Technol.* **127** 83–9

[31] Peirce D, Shih C F and Needleman A 1984 A tangent modulus method for rate dependent solids *Comput. Struct.* **18** 875–87
[32] Hughes T J and Winget J 1980 Finite rotation effects in numerical integration of rate constitutive equations arising in large-deformation analysis *Int. J. Numer. Methods Eng.* **15** 1862–7
[33] Zienkiewicz O and Taylor R 1991 *The Finite Element Method* vol 1 (London: Butterworth-Heinemann) pp 128–32
[34] Jaganathan Anuja 2019 Numerical studies on the mechanical response of shape memory alloys *PhD Thesis (under preparation)* Indian Institute of Science, Bangalore, India
[35] Jacobus K, Sehitoglu H and Balzer M 1996 Effect of stress state on the stress-induced martensitic transformation in polycrystalline Ni–Ti alloy *Metall. Mater. Trans.* A **27** 3066–73
[36] Mirzaeifar R, DesRoches R, Yavari A and Gall K 2013 On superelastic bending of shape memory alloy beams *Int. J. Solids Struct.* **50** 1664–80
[37] Kumar K S 1998 Finite element modeling of contact problems *ME Thesis Dissertation* Indian Institute of Science, Bangalore, India
[38] Mesarovic S D and Fleck N A 1999 Spherical indentation of elastic-plastic solids *Proc. R. Soc. London* A **455** 2707–28
[39] Hughes T J 1980 Generalization of selective integration procedures to anisotropic and nonlinear media *Int. J. Numer. Methods Eng.* **15** 1413–8
[40] Moran B, Ortiz M and Shih C 1990 Formulation of implicit finite element methods for multiplicative finite deformation plasticity *Int. J. Numer. Methods Eng.* **29** 483–514
[41] Johnson K L 1987 *Contact Mechanics* (Cambridge: Cambridge University Press)
[42] Shastry V and Ramamurty U 2013 Simultaneous measurement of mechanical and electrical contact resistances during nanoindentation of NiTi shape memory alloys *Acta Mater.* **61** 5119–29